Engineering Structures 289 (2023) 116234

Contents lists available at ScienceDirect

Engineering Structures

journal homepage: www.elsevier.com/locate/engstruct

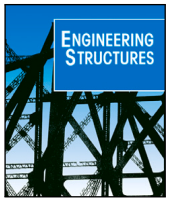

A numerical model for non-linear shear behavior of high damping rubber bearings

José A. Gallardo [a,b,*], Juan C. de la Llera [a,b], José I. Restrepo [c], Michelle Chen [c]

[a] Department of Structural and Geotechnical Engineering, Pontificia Universidad Catolica de Chile, Santiago, Chile
[b] Research Center for Integrated Disaster Risk Management (CIGIDEN), Santiago, Chile
[c] Department of Structural Engineering, University of California, San Diego, 9500 Gilman Dr., La Jolla, CA 92093, USA

ARTICLE INFO

Keywords:
Seismic isolation
High damping rubber bearing
Scragging and Mullins effect
Stiffness degradation
HDRB parameter estimation

ABSTRACT

The dynamic behavior of isolated structures is strongly controlled by the force–deformation constitutive behavior of the isolators. Among the different types of existing isolation devices, High Damping Rubber Bearings (HDRBs) are commonly used in practice, which behavior is highly non-linear and difficult to model analytically. Consequently, this article proposes a simple, but sufficiently accurate, mathematical model for simulating the non-linear shear behavior of HDRBs under large deformations, and an estimation procedure for its parameter values using the geometrical features and mechanical characteristics of the device. First, we briefly describe the phenomena observed in the experimental test data, as well as other phenomena not observed within the range of experimental deformations. Then, the mathematical formulation is presented, which is based on the consideration of two components connected in parallel, a hyperelastic spring and a dissipative component. The governing equation for the former is derived from the expanded formulation of the Mooney–Rivlin model for isotropic hyperelastic materials, and the latter from a Bouc-Wen model with hardening. A novel model is included to account for stiffness degradation, including scragging and Mullins effects, which is developed from experimental data of 924 tested devices. The proposed model fits well the experimental test results of HDRBs with different geometric features and material properties. Based on the evolution laws for the different variables, the model can be successfully used in structural dynamic analysis. To facilitate model calibration, a statistical estimation procedure is proposed to reduce the 17 force–deformation constitutive model parameters of the isolator to 9 unknown parameters, which are computed from the geometric features of the device and mechanical characteristics of the rubber material. This makes the calibration of the force–deformation constitutive model parameters feasible. The estimation procedure successfully predicts the behavior of an average device within a batch of HDRBs, showing good agreement with two different experimental datasets.

1. Introduction

Seismic isolation is an effective technique used worldwide to protect equipment, structural and non-structural components of buildings in high seismicity zones. The technique has been used to retrofit historical buildings [1–3], as well as in the design of new structures [4]; the latter with a strong emphasis in essential facilities. During the last two decades, the use of seismic isolation has increasingly become more popular due to its good performance during large earthquakes [5,6]. The geometric arrangement of isolators between the superstructure and substructure seeks two principal goals: to uncouple as much as possible the dynamics of the superstructure from the base motion by lengthening the periods of the isolated structure relative to the predominant frequencies of the expected ground motions, and to increase the internal damping in the system. Thus, the isolators work as a mechanical filter, which reduces accelerations and relative deformations in the superstructure.

Different isolation devices are available, such as elastomeric bearings with and without a lead-core [7]; frictional pendulum systems in different versions (double [8], triple [9], quintuple [10]); kinematic self-centering devices [11,12], among others. Nowadays, elastomeric or rubber bearings, including High Damping Rubber Bearings (HDRBs) and lead-core rubber bearings, are probably the most widely used isolation devices in practice. They are produced by intercalating and vulcanizing rubber layers with thin steel shims. The behavior of the

* Corresponding author at: Department of Structural and Geotechnical Engineering, Pontificia Universidad Catolica de Chile, Santiago, Chile.
E-mail addresses: jogallardo@uc.cl (J.A. Gallardo), jcllera@ing.puc.cl (J.C. de la Llera), jrestrepo@ucsd.edu (J.I. Restrepo), drchen@mcese.com (M. Chen).

https://doi.org/10.1016/j.engstruct.2023.116234
Received 8 August 2022; Received in revised form 28 March 2023; Accepted 25 April 2023
Available online 16 May 2023

rubber, and consequently of the device, is highly non-linear, and it is difficult to model analytically. Hence, this research focuses on HDRBs.

Several numerical studies have been developed to simulate the force–deformation constitutive behavior of HDRBs [13–18]. In general, as of today, the theory of continuum mechanics cannot accurately reproduce the behavior of these devices, and since micro-models are computationally very costly, phenomenological macro-models are preferred. Most of the macro-models decompose the force–deformation response into a hyperelastic (or elastic) and a dissipative component to reproduce the overall cyclic behavior of the devices. Additionally, the stiffness degradation of the rubber is an important characteristic that needs to be included in the models, which is a challenge. This has been done previously by some authors [19–21], but the resulting models are still very complex and cumbersome to calibrate with experimental data.

Currently, design standards [22–24] allow modeling HDRBs using an equivalent linear elastic-viscous damping or a bi-linear hysteretic model, depending on the analysis procedure. Both of these models neglect phenomena that are inherent to the device, such as stiffness degradation, temporary hardening, and the characteristics of the unloading branch. ASCE7-16 [22] includes the effect of stiffness degradation into an uncertainty factor reflected in the computation as an upper and lower bound for the force–deformation constitutive relationship of the device. Also, the behavior of isolated structures is studied mostly by modeling the isolation devices by the approaches accepted in the standards [25,26], and just sometimes using more sophisticated models [27,28]. However, to the best of the authors knowledge, no previous research includes all the effects of temporary hardening and anisotropic stiffness degradation (scragging and Mullins effect), and P-Δ effects. One important reason to avoid the use of more complex isolator models, which include all of those phenomena, is the difficulty of the parameter calibration.

Isolated buildings are becoming taller, and improved isolator modeling is necessary. Overall, the accuracy in predicting the dynamic behavior of a seismically isolated structure is strongly conditioned by the response of the force–deformation constitutive behavior of the seismic isolators. Therefore, an efficient and simpler numerical model capable of simulating the non-linear behavior of the isolators is proposed herein. Consequently, this article aims to: (a) propose a sufficiently accurate numerical model for the shear behavior of HDRBs under large strains which is numerically efficient and simpler to implement and; (b) predict its parameters from the geometric features of the devices and the mechanical properties of the elastomeric material. This article is organized into five sections besides this introduction. Section 2 describes the phenomenological behavior of the devices subjected to axial load and lateral cyclic deformation histories, a brief description of the most commonly observed phenomena is also presented. Section 3 presents the mathematical formulation of the proposed model, the derivation of the equations, and the evolution laws for the strain-dependent variables. Section 4 presents a statistical analysis to reduce the number of variables by considering some parameters as constant, while searching for a relationship between the other model parameters, mechanical properties of the material, and geometric characteristics of the device. Then, Section 5 depicts the results of the analytical model and compare these with experimental test results. The model captures the overall behavior of HDRBs, and the parameter estimation model for the force–deformation response of an average device in a batch. Finally, Section 6 presents the numerical implementation of the proposed model, and Section 7 discusses the relevant characteristics of the model and presents the conclusions of this study.

2. Phenomenological behavior of a HDRB

HDRBs are produced by intercalating and vulcanizing rubber layers with 2–3 mm thickness steel shims, as shown schematically in Fig. 1. Since the in-plane stiffness of the steel shims is much larger than the shear stiffness of the elastomer pads, it is customary to assume that the

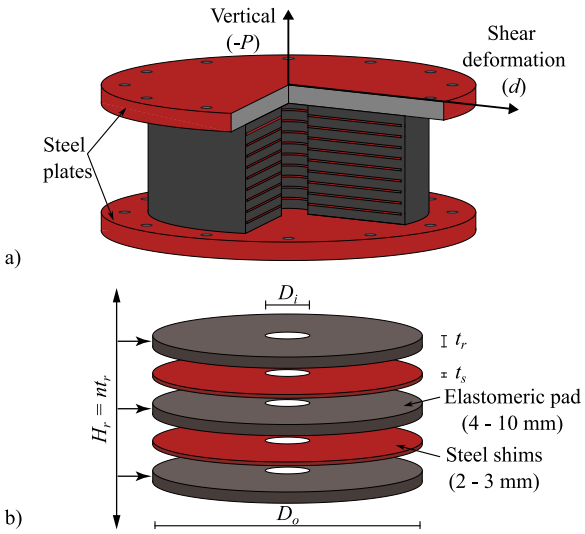

Fig. 1. Sketch of the geometry and internal structure of an annular HDRB: (a) device; (b) isolator assemblage and dimensions.

constitutive behavior of the rubber is the one that controls the overall behavior of HDRBs. The steel shims restrict the free lateral expansion of the rubber and thus increase the vertical stiffness of the steel-rubber composite material. The rubber layers provide large shear flexibility to the device. Consequently, the behavior of the device is highly non-linear due primarily to the characteristics of the force–deformation constitutive behavior of the rubber.

Therefore, since the behavior of seismically isolated structures is strongly dependent on the force–deformation response of the isolators, most design standards require testing prototype isolation devices to validate the quality and robustness of their properties under loads and displacements corresponding to the maximum considered earthquake. Additionally, the consistency of the nominal and actual properties is evaluated by testing all isolators used in construction. This testing process has left a large amount of data in this research team, which is helpful for studying in detail the behavior of devices under the expected deformations. This database is composed mostly of the result of quality control tests for several building projects. It includes experimental results of over 2000 HDRBs that were carried out over a period of about 20 years [29]. Each device was tested under design load conditions, which included a constant axial load and cyclic lateral deformation pattern. The data includes devices with annular shapes with a wide range of inner and outer diameters (D_i and D_o, respectively), elastomer layer thicknesses (t_r), number of elastomer layers (n), total height of rubber (H_r), and shear modulus of the elastomeric material (G). In order to study the general phenomenological behavior of HDRBs, a subset of experimental results composed of 924 devices was selected from the experimental dataset [29]. This selected subset considered: (i) results with reduced instrumentation and measurement inconsistencies; (ii) results of devices with different material and geometric properties, such as shear modulus of rubber (G), inner diameter (D_i), outer diameter (D_o), thickness of the rubber layers (t_r), total height of rubber (H_r), and compressive load (P); (iii) a minimum number of devices with the same nominal properties to account for the inherent uncertainty of the devices; and (iv) the same number of testing strain levels (four) and cycles per strain level (seven) for all tests. Thus, the subset contains results of 41 different device designs, all from the same manufacturer; a summary of the key parameters is presented in Table 1. Fig. 2 shows the shear force–deformation response of a single HDRB, which contains some of the interesting characteristics of the devices; this example is representative of the database. It is relevant to note that all tests have been performed at a fixed frequency of about 0.08 Hz, and since time

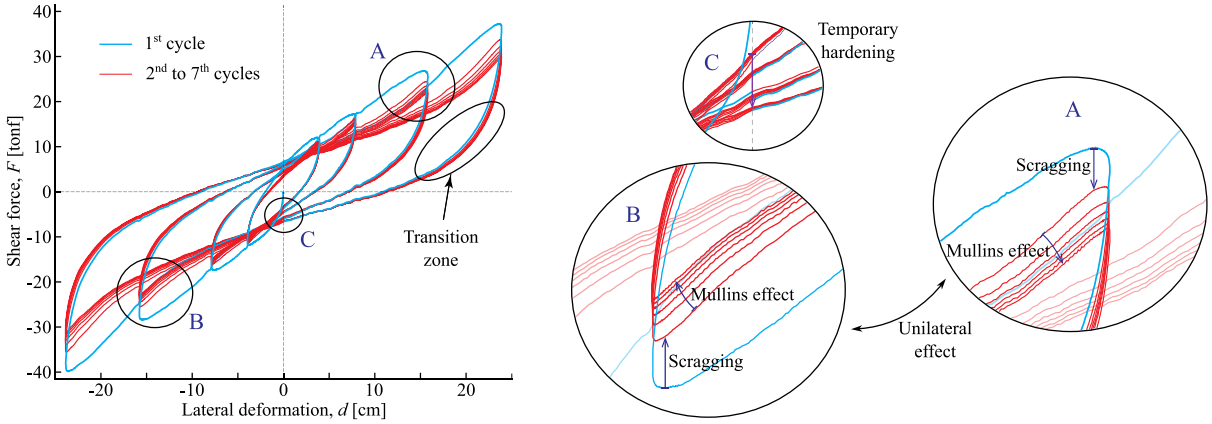

Fig. 2. Characteristics of the shear force–deformation response of an HDRB.

Table 1
Parameters summary of the subset of devices.

	D_i cm	D_o cm	D_i/Do [–]	t_r cm	H_r cm	S[a] [–]	G kgf/cm^2	γ_{max}[b] [–]	σ[c] [kgf/cm^2]
Minimum	10.0	60.0	0.13	0.6	12.6	14.1	4.0	0.77	41.65
Maximum	15.0	100.0	0.25	0.8	25.9	29.2	8.0	1.65	205.99

[a]Shape factor $\left[S = \left(D_o - D_i\right)/4t_r\right]$.
[b]Maximum shear strain ($\gamma = d/H_r$).
[c]Axial compressive stress $\left[\sigma = P/A\right]$, where A is the section area of the rubber compound.

data is not available in the database, no rate-dependent effects will be considered herein.

The experimental results shown in Fig. 2 correspond to a device subjected to four different strain levels with seven full cycles at each strain level. First, notice the stiffness degradation observed during cycles at the same strain level. The first cycle at each strain level is colored in blue, while the following cycles are colored in red. Most of the stiffness degradation occurs during the first cycle, and though it continues in the following cycles, the decrements in stiffness at the same strain level are proportionally less at each consecutive cycle. In the literature, this stiffness degradation is commonly denoted as Mullins effect [30], which is defined as the softening of like-rubber materials at elongations smaller than the previous deformations; a detailed explanation of this phenomenon can be found elsewhere [30]. However, of is customary to distinguish between stiffness degradation during the first and subsequent cycles. This distinction is present in the literature [20] and also used here. The term "scragging" is used to describe the long-term degradation reflected in the stiffness degradation during the first cycle. In contrast, the term "Mullins effect" refers to the short-term degradation, or the stiffness degradation in all subsequent cycles. Also, despite the significant stiffness degradation during loading at maximum positive strain for all cycles, the unloading branches are essentially identical. The curved zone located right after unloading is commonly denoted as the transition zone (see Fig. 2). Another interesting feature of these devices is the symmetric response in the positive and negative deformation directions. Thus, the deformation history in the negative direction has no memory of the response in the positive direction, and vice versa. Therefore, since the stiffness degradation occurs at each positive or negative deformation direction independently, this phenomenon is labeled as unilateral (or anisotropic). Furthermore, the force of the device at zero deformation differs for each strain level, becoming larger for target higher strain levels (Fig. 2). Other experimental studies with decreasing strain levels have shown that this hardening at zero deformation is temporary and decreases as the prior last strain level decreases (e.g., [31]). The term temporary hardening will be used herein to refer to this phenomenon. In this example, four different force levels at zero deformation can be identified as corresponding to the four different target maximum strain levels. However, this temporary hardening cannot increase indefinitely with increasing strains, and so its value is bounded. The evolution law of this temporary hardening depends on the prior last maximum shear strain, while its bound is a material property.

There are also other well-known characteristic phenomena of HDRBs, such as cavitation [13,32,33] and vertical instability [34–36]. However, the experimental measurement of setup the database was not aimed to evaluate these phenomena, and hence it cannot be considered in the formulation of the proposed shear response of HDRB model. However, in a sequel article, the authors incorporate these phenomena in the extension of the proposed model to the case of multi-axial behavior.

3. Mathematical formulation

A classical assumption about the behavior of HDRBs is that the force–deformation response can be decomposed into a hyperelastic component and a dissipative component. Consequently, the experimental response of each device of the subset presented in the previous section was separated by cycles, and each cycle in its hyperelastic and dissipative component. The hyperelastic component corresponds to the backbone reference of the cycle (the curve throughout the center or axe of the cycle), while the dissipative component is obtained by the subtraction of the hyperelastic component from the total force (Fig. 3). From the results of this decomposition, the following observation are established: (i) it is apparent that only the hyperelastic component presents stiffness degradation (Fig. 3b); (ii) the dissipative component keeps its yield force in different cycles at the same maximum strain, but increases the value of force as the maximum strain increases (Fig. 3c); and (iii) stiffness degradation of the hyperelastic component is produced sharply during the unloading branch (Fig. 3d). Thus, the mathematical model proposed accounts for temporary hardening and stiffness degradation; and the latter includes scragging and Mullins effect. The unilateral (anisotropic) degradation effect noted in the experimental tests, and the smooth unloading transition zone in the force–deformation constitutive behavior are also considered in the formulation.

Mathematically, the proposed model is based on the idealization of two components working in parallel (see Fig. 3a), where the total lateral force of the device is equal to the sum of the forces of the hyperelastic and dissipative component, i.e.,

$$F = F_h + F_d. \tag{1}$$

In Eq. (1), F, F_h, and F_d, are the total shear force of the device, the shear force of the hyperelastic spring, and the shear force of the dissipative element, respectively. This decomposition enables us to study

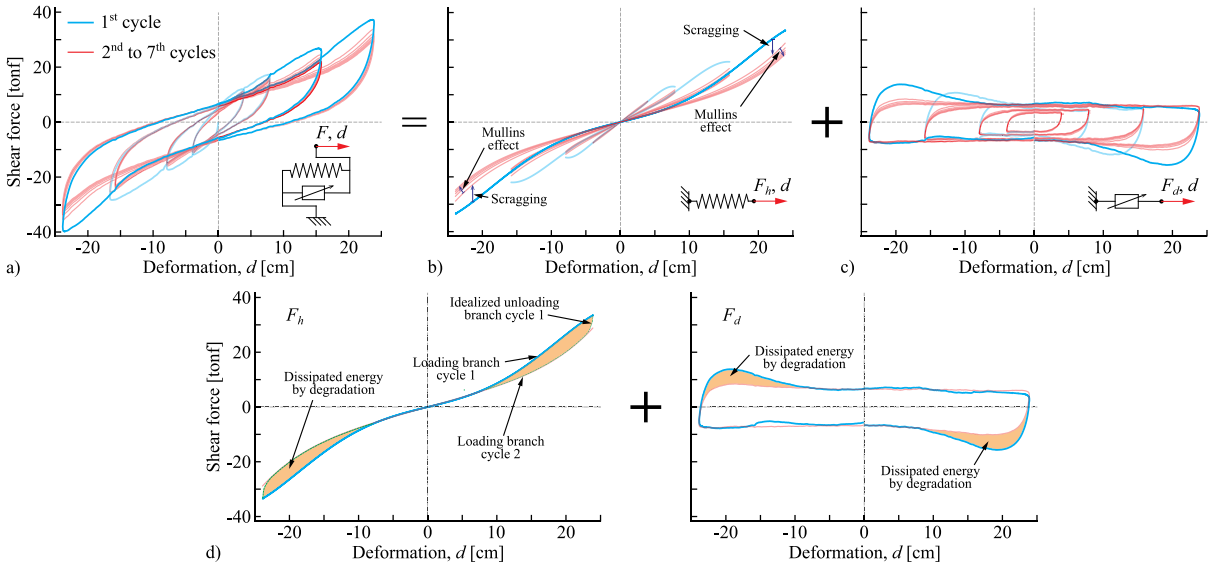

Fig. 3. Decomposition of (a) the elastomeric bearing response into (b) a hyperelastic and (c) a dissipative component; and, (d) idealization of the stiffness degradation and dissipated energy balance.

the phenomena by looking at each term separately. The derivation of the equations that govern the response of both components is presented next.

3.1. Hyperelastic component

The basic characteristics of the force–deformation constitutive behavior of rubber-like materials are usually modeled in continuum mechanics by the theory of hyperelasticity, considering also isotropy and incompressibility. A hyperelastic material is one in which stress can be derived from a strain energy density function. The general form of this strain energy function for an incompressible isotropic hyperelastic material [37] is

$$W^* = W(I_1, I_2) - c_0(J-1), \tag{2}$$

where I_1, and I_2 are the principal strain invariants of the left Cauchy–Green deformation tensor $\boldsymbol{B}$, defined as $\boldsymbol{B} = \boldsymbol{F}\boldsymbol{F}^T$, where $\boldsymbol{F}$ is the deformation gradient tensor; c_0 is an indeterminate Lagrangian multiplier, identified as a hydrostatic pressure; and $J = \det(\boldsymbol{F}) = 1$ represents the incompressibility constraint. The strain invariants are defined as

$$I_1 = \mathrm{tr}(\boldsymbol{B}), \tag{3a}$$

$$I_2 = \frac{1}{2}\left[\mathrm{tr}(\boldsymbol{B})^2 - \mathrm{tr}\left(\boldsymbol{B}^2\right)\right], \tag{3b}$$

where $\mathrm{tr}(\bullet)$ and $\det(\bullet)$ are the trace and determinant of $\bullet$, respectively.

The constitutive equation for the first Piola-Kirchhoff stress tensor $\boldsymbol{P}$ is defined by differentiating Eq. (2) with respect to the deformation gradient tensor $\boldsymbol{F}$, and can be expressed as

$$\boldsymbol{P} = \frac{\partial W}{\partial \boldsymbol{F}} - c_0\boldsymbol{F}^{-T}. \tag{4}$$

More details about the complete formulation and the derivation of the first Piola-Kirchhoff stress tensor $\boldsymbol{P}$ can be found elsewhere [37].

Several hyperelasticity theories have been presented, and several strain energy functions proposed to represent the behavior of elastomeric materials (e.g., Mooney–Rivlin, Ogden, Arruda-Boyce, Yeoh, among others [37,38]). The expanded formulation for the strain energy function presented by Mooney [39] and Rivlin [40] is used herein, which is defined by

$$W(I_1, I_2) = \sum_{p,q=0}^{\infty} c_{pq}\left(I_1 - 3\right)^p\left(I_2 - 3\right)^q, \tag{5}$$

where the coefficients c_{pq} are material parameters. It is worth mentioning that the requirement of zero energy at the reference configuration is met only if c_{00} equals to zero. Thus, considering the strain energy density W presented in Eq. (5), the first Piola-Kirchhoff stress tensor $\boldsymbol{P}$ defined in Eq. (4) can be expressed as

$$\boldsymbol{P} = \sum_{p,q=0}^{\infty} 2\left(I_1 - 3\right)^p\left(I_2 - 3\right)^q\left[(p+1)c_{(p+1)q}\boldsymbol{F} + (q+1) \times c_{p(q+1)}\left(I_1\boldsymbol{F} - \boldsymbol{B}\boldsymbol{F}\right)\right] - c_0\boldsymbol{F}^{-T}. \tag{6}$$

Since the predominant deformation of HDRBs is in shear, and the aim of this work is to approximate the shear behavior of rubber bearings, a reasonable assumption is to consider a pure shear deformation state on the derivation of these equations. In that case, the deformation gradient tensor $\boldsymbol{F}$, and the corresponding left Cauchy–Green deformation tensor $\boldsymbol{B}$ are

$$\boldsymbol{F} = \begin{bmatrix} 1 & \gamma & 0 \\ 0 & 1 & 0 \\ 0 & 0 & 1 \end{bmatrix}, \qquad \boldsymbol{B} = \begin{bmatrix} \gamma^2+1 & \gamma & 0 \\ \gamma & 1 & 0 \\ 0 & 0 & 1 \end{bmatrix}, \tag{7}$$

where γ is the shear strain of the elastomeric compound ($\gamma = d/H_r$). Then, introducing the condition of a pure shear deformation state (Eq. (7)), and considering a hydrostatic pressure equal to zero ($c_0 = 0$), the shear component of the first Piola-Kirchhoff stress tensor (Eq. (6)) is

$$\boldsymbol{P}(1,2) = c_{00} + 2(c_{01} + c_{10})\gamma + 4(c_{02} + c_{11} + c_{20})\gamma^3 + 6(c_{03} + \cdots)\gamma^5 + 8(c_{04} + \cdots)\gamma^7 + 10(c_{05} + \cdots)\gamma^9 + \cdots. \tag{8}$$

It is worth noting that for this deformation state, the shear component of the first Piola-Kirchhoff stress tensor, and the shear component of the commonly used Cauchy stress tensor are equal.

Given the shape of the hyperelastic component of HDRBs (Fig. 3b), and calibrating the parameters of Eq. (8) to match the hyperelastic component of the experimental results, it can be shown that the terms of power of γ higher than five have a negligible contribution to the shear component. Therefore, the shear stress of the material truncated after the third term can be expressed as

$$\boldsymbol{P}(1,2) \approx 2\left(c_{01} + c_{10}\right)\gamma + 4\left(c_{02} + c_{11} + c_{20}\right)\gamma^3 + 6\left(c_{03} + c_{12} + c_{21} + c_{30}\right)\gamma^5. \tag{9}$$

Considering now that the shear force of the device is the integral of the shear stress $\boldsymbol{P}(1,2)$ across the cross section A of the isolator, and

assuming that the shear stress is constant across the area given the small thickness of the elastomeric pads, the total shear force F_h of the device is

$$F_h \approx a_1\gamma - a_2\gamma^3 + a_3\gamma^5, \tag{10}$$

where the a_i terms are the sum of the corresponding material c_{pq} parameters multiplied by the area A of the isolator cross-section. Assuming also that the degradation factors for scragging and Mullins effect are controlled by the constants of the hyperelastic component, the values of a_i can be expressed as

$$a_1 = 2\left(c_{01} + c_{10}\right)\left(f_{s1}f_{m1}\right)A = f_{s1}f_{m1}a_{10}, \tag{11a}$$

$$a_2 = 4\left(c_{02} + c_{11} + c_{20}\right)\left(f_{s2}f_{m2}\right)A = f_{s2}f_{m2}a_{20}, \tag{11b}$$

$$a_3 = 6\left(c_{03} + c_{12} + c_{21} + c_{30}\right)\left(f_{s3}f_{m3}\right)A = f_{s3}f_{m3}a_{30}, \tag{11c}$$

where f_{si} and f_{mi} are the i-th degradation factors that represent the scragging and Mullins effect, respectively, whose values depend on the material; and a_{i0} is the i-th hyperelastic constant, which depends on the mechanical properties of the virgin material and the cross-section area of the device. The computation of the values for f_{si} and f_{mi} is detailed later in this paper.

3.2. Dissipative component

The energy dissipation capacity of the device is explicitly modeled by the dissipative component, which controls the smooth transition zone and temporary hardening. A numerical phenomenological model capable of considering both characteristics is the Bouc-Wen model with hardening as proposed by Karavasilis et al. [41]. This model results from the combination of an elastic and an elastic perfectly-plastic component in parallel. The elastic component of the model is neglected since its behavior is already captured by the hyperelastic component described previously, and hence the dissipative component force F_d is defined as

$$F_d = f_y z, \tag{12}$$

where f_y is the yield force and z is a dimensionless hysteretic parameter governed by the evolution law [41]

$$\dot{z} = \frac{k}{f_y}\dot{\gamma}\left[1 - |z|^{\eta}\left(\beta\,\mathrm{sgn}(\dot{\gamma}z) + \alpha - \Phi\,\mathrm{sgn}(\dot{\gamma})\left(\mathrm{sgn}(z) + \mathrm{sgn}(\dot{\gamma})\right)\right)\right], \tag{13}$$

where $\dot{\gamma}$ is the shear strain rate; k is a parameter defined by the initial stiffness of the device k_i multiplied by the total height of rubber H_r ($k = k_i * H_r$); β and α are parameters that control the shape of the cycle and satisfy the relationship $\beta + \alpha = 1$; η controls the sharpness of the smooth transition from the elastic to the inelastic zone; Φ controls the temporary hardening; and sgn(•) is the signum function.

Although the model is capable of considering different levels of temporary hardening in each direction, it is assumed identical for both deformation directions. The parameter Φ is determined by

$$\Phi = \Phi_{max}\left[1 - \exp\left(-P_{\Phi}\left|\frac{\gamma_{pl}}{\gamma_y}\right|\right)\right], \tag{14}$$

where Φ_{max} represents the maximum possible value of Φ; P_{Φ} is the parameter that controls the temporary hardening rate; γ_y is the yield shear strain (f_y/k); and γ_{pl} is the plastic shear strain corresponding to the last change of load direction. Detailed information about evolution laws of different variables of the Bouc-Wen model with hardening can be found elsewhere [41].

3.3. Stiffness degradation

The experimental results show that the effect of stiffness degradation in the shear force–deformation response (Fig. 1) cannot be neglected since it represents an important decrease in the force of HDRBs at the same strain level for each consecutive cycle. Some researchers argue that stiffness degradation occurs in both, the hyperelastic and dissipation components [20]. However, decomposing the experimental responses in their components (e.g., Fig. 3), it is apparent that the hyperelastic component presents stiffness degradation, while the dissipation component keeps its yield force (f_y) for a constant strain level, and it increases (temporary hardening) as the strain level increases. Consequently, the stiffness degradation is included herein only through the parameters a_1, a_2, and a_3 of the hyperelastic component. Then, considering Eq. (11), the stiffness degradation factors can be expressed as

$$\frac{a_i}{a_{i0}} = f_{si}f_{mi}. \tag{15}$$

After separating the response of the 924 HDRBs in the hyperelastic and dissipative components and calibrating the parameters of Eq. (10) to match the hyperelastic components, the values of parameters a_i were estimated for each cycle and strain level. Assuming that the hyperelastic parameter values of the first cycle of the first strain level correspond to the parameters of the virgin material (a_{i0}), the degradation parameters for the rest of the cycles and strain levels were estimated using Eq. (15).

Fig. 4 shows schematically the stiffness degradation idealization in the shear force–deformation constitutive relationship of HDRBs and box-plots of the estimated degradation factors $f_{si}f_{mi}$. It is apparent from the figure that each degradation coefficient evolves differently. Also, there is a high dispersion (length of bars) of the degradation factors $f_{s2}f_{m2}$ and $f_{s3}f_{m3}$ at small strain levels, which is indicative of the small influence of these factors in that range of deformations. In terms of the scragging, $f_{s1}f_{m1}$ shows an increase during loading of the first cycle at each shear strain level and in the unloading branch between the first and second cycles. Fig. 4a shows the total scragging for which the force of the hypothetical cycle without scragging during loading is always larger than the actual response. This can be observed by comparing the values of degradation factors occurring at cycles 8 and 15 (the effect in cycle 22 is less evident). The total scragging at these shear strains corresponds to the sum of the drop in force of the previous and next cycle, respectively. Notice that for $f_{s2}f_{m2}$ and $f_{s3}f_{m3}$ the Mullins effect, which is represented by the purple little bar, is negligible, which means that for the same shear strain level, $f_{si}f_{mi}$ remains essentially constant for all cycles. Thus, f_{m2} and f_{m3} are considered constant and equal to 1. The opposite occurs with $f_{s1}f_{m1}$, for which the degradation due to the Mullins effect is evident.

3.3.1. Scragging effect

As defined in the previous section, scragging is the long-term stiffness degradation of the hyperelastic component and is reflected between the first and second cycle at each strain level (see Fig. 4). The function that represents this phenomenon must equal one when the device has no previous deformation and converge asymptotically to zero (or any other value between zero and one) as the strain approaches infinite. Because this decrease must be smooth, the expressions for the degradation factors due to scragging are defined as

$$f_{s1} = \exp(-C_1\gamma_s^{p_1}), \tag{16a}$$

$$f_{s2} = f_{s1}\exp(-C_2\gamma_s^{p_2}), \tag{16b}$$

$$f_{s3} = f_{s1}\exp(-C_3\gamma_s^{p_3}), \tag{16c}$$

where C_i are material parameters, and the p_i are constants that control the decay of the function for each term of the hyperelastic component, a_i, $i = 1, 2, 3$, for which the unique value that requires an evolution law in Eq. (16) is the internal variable γ_s, defined as the corresponding shear strain for the scragging effect. Three important assumptions are considered to develop this evolution law: (i) γ_s is always less than or equal to the value of γ at which the previous cycles were performed; (ii) for the first loading cycle at a new shear strain γ, γ_s evolves slower than the increase experienced by γ; and (iii) for the unloading branch, γ_s evolves quickly to achieve the full scragged state at that level of γ.

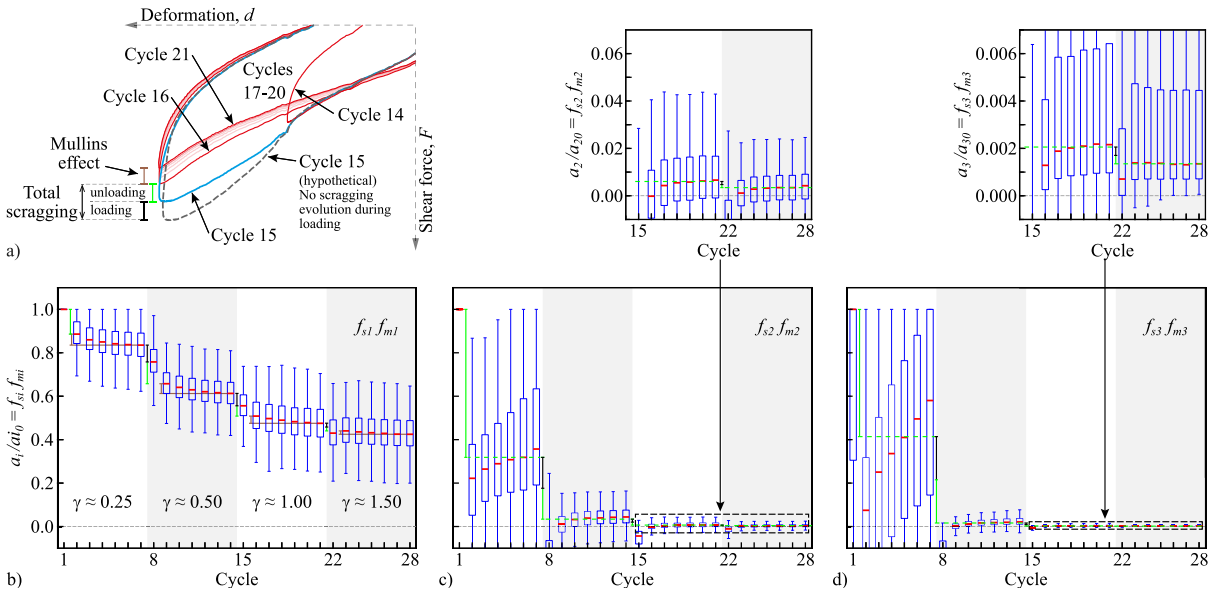

Fig. 4. Evolution of the degradation factors with the number of cycles: (a) sketch of the degradation in the force–deformation response; and box-plots of the estimated experimental values for (b) $f_{s1} f_{m1}$ (c) $f_{s2} f_{m2}$, and (d) $f_{s3} f_{m3}$.

These assumptions are based on the idealization presented in Figs. 3d and 4a. Therefore, the proposed value for γ_s is

$$\gamma_s^{\pm} = \min\left(\gamma_{hp}^{\pm}, \gamma_{s(trial)}^{\pm}\right), \tag{17}$$

where $\gamma_{hp}^{\pm}$ is the peak strain value of γ at which the previous cycles were performed, and $\gamma_{s(trial)}^{\pm}$ is the projected γ_s, which is computed from the previous value of γ_s and a rate of change that depends on the loading state

$$\dot{\gamma}_{s(trial)}^{\pm} = \begin{cases} \dfrac{|\dot{\gamma}|}{2}, & \text{for loading} \\ 4\,|\dot{\gamma}|, & \text{for unloading.} \end{cases} \tag{18}$$

The superscript $^{\pm}$ reflects the unilateral effect, which means that the increment of γ_s occurs in each direction independently. The factors of 1/2 and 4 for loading and unloading are heuristic and proposed based on the experimental results.

3.3.2. Mullins effect

The short-term stiffness degradation of the hyperelastic component that occurs in the second and subsequent cycles is defined as the Mullins effect. Analogous to scragging, the function that describes this decay must equal one when the elastomer has no previous deformation and be asymptotic to zero (or any other value between zero and one) as the number of cycles increases. However, as stated before such effect is only present in the f_{m1} coefficient, while for $f_{m2} = f_{m3} \approx 1$. Because the trends of f_{m1} resemble those of f_{s1}, the proposed evolution function for the Mullins effect factor is

$$f_{m1} = exp(-C_m \gamma_m^{p_m}), \tag{19}$$

where C_m is a material parameter, p_m is a constant that controls the decay of the function, and γ_m is the cumulative strain. Similar to scragging, the Mullins phenomenon shows a unilateral effect. Hence, the γ_m increments are independent in each direction. Considering that the Mullins factor only increases during unloading, the evolution law for γ_m is defined by the increase rate

$$\dot{\gamma}_m^{\pm} = \begin{cases} 0, & \text{for loading} \\ |\dot{\gamma}|, & \text{for unloading.} \end{cases} \tag{20}$$

The complete model is then defined by a total of 17 parameters: three for the hyperelastic component (a_{10}, a_{20}, a_{30}), four for the dissipative component (γ_y, f_y, β, η), two for defining the temporary hardening (Φ_{max}, P_Φ), six for defining scragging (C_1, p_1, C_2, p_2, C_3, p_3), and two for defining the Mullins effect (C_m, p_m). Consequently, the calibration of these parameters can be difficult and time-consuming. Thus, a reduction in the number of parameters is presented next, as well as an estimation model for the rest that depend on the geometry of the device and material properties.

4. Prediction model for the parameter values

The mathematical model proposed needs to be calibrated from experimental tests. In design, however, the results of such tests are not available and even if they were, parameter calibration would be cumbersome. Thus, this section aims to estimate the model parameter values from the general geometric and material characteristics of the device, using a base expansion and linear regressions. The aim of the prediction model is twofold: to estimate the parameter values for the behavior of an average device of a set of HDRBs with the same nominal properties, which can be useful to predict the overall behavior of seismically isolated structures; and to provide a set of initial parameters for the calibration of the proposed model to match the experimental response of HDRBs. Then, the results of this prediction model can be used depending on the available data.

First, the 17 parameter values were estimated to match the experimental results of the 924 devices of the subset. The calibration process considered the minimization of the squared difference between the measured and model forces for each sampled deformation, i.e., the objective was to

$$\text{minimize}\left\{\sum_{i=1}^{s}\left(f_i^t - f_i^m\right)^2\right\}, \tag{21}$$

where s is the number of sampled deformations, and f_i^t and f_i^m are the forces corresponding to the i-th sampled deformation of the test and model results, respectively. Force was preferred over dissipated energy per cycle as a measure of the error since the latter equalizes the area without explicitly considering the shape of the cycle, while the force error seeks equality at each measured point and indirectly enforces to preserve the shape of the response cycle [18].

The minimization procedure was automated using the Covariance Matrix Adaptation Evolution Strategy (CMA-ES) proposed by Hansen

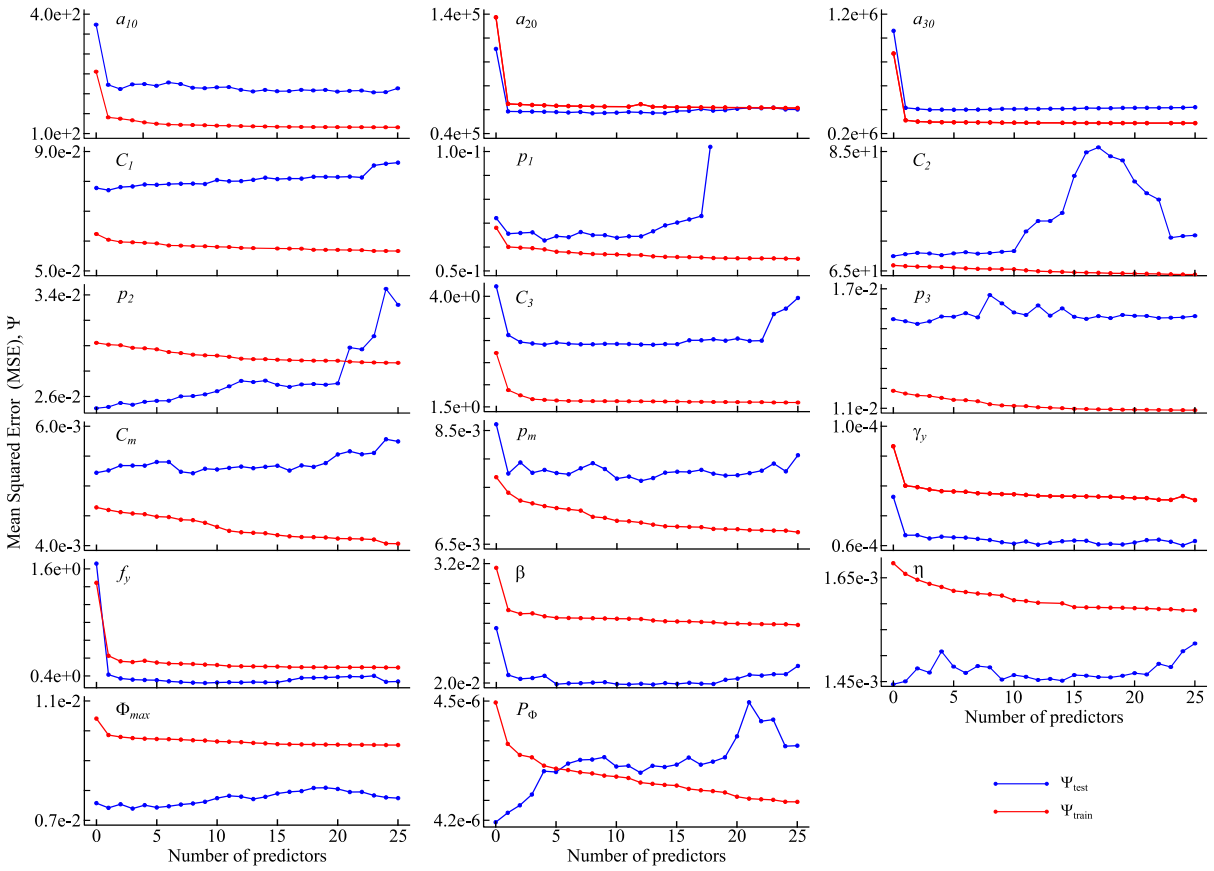

Fig. 5. Comparison between training (Ψ_{train}) and validation (Ψ_{test}) mean squared error.

and Ostermeier [42], and was implemented as presented in the literature [43]. This algorithm has already been used in structural engineering in the identification of structural systems [44,45]. The method uses the previously stated demands for the evolution path of mutations rather than using arbitrary normal mutations to improve the search [42]. However, two small modifications were introduced to the base algorithm: (i) the first element in each family mutation step is the best-fitted set of the previous step; and (ii) the maximum variation for each mutation of the parameters is established as a function of the values corresponding to the best-fitted set in the previous step. The first modification was to ensure that in each step, the error is less than or equal to the error in the previous step, while the second modification was due to the different magnitudes of parameters and the unbounded values. The CMA-ES algorithm considered the following: a maximum variation of each step of 25%; 20 descendants in each step; a maximum number of 2000 iterations (or descendants), which means 100 steps; and only the best descendant was considered for recombination.

After the calibration process, the response of the 924 HDRBs was simulated with the proposed model. Thus, the result of the calibration process is 924 sets for the 17 model parameters, where each set corresponds to a different device. Two randomly selected examples of these calibration results are presented in Fig. 7. The aim of the following subsections is to analyze and predict the values of the 17 model parameters; and hence, this calibration is essential for the prediction model since these data are used for the calibration and test of the model.

4.1. Base expansion

Six geometric properties, one material parameter, and one loading condition are considered as predictors or explanatory variables for the prediction model. These are the outer diameter of the bearing (D_o in cm), inner diameter (D_i in cm), shape factor (S, dimensionless), number of rubber layers (n, dimensionless integer), the thickness of rubber layers (t_r in cm), the total height of rubber (H_r in cm), shear modulus (G in tonf/cm^2) of the elastomeric material and the axial load (P in tonf). In addition, two device properties are also considered: nominal shear stiffness ($K_h = AG/H_r$ in tonf/cm, where A is the cross section area of the rubber layers), and the compressive stress ($\sigma = P/A$ in tonf/cm^2). All of these parameters were determined for each device.

Linear regression was used to estimate the parameter values of the numerical model, which limitation is that the method can only approximate the value of the response variable using linear combinations of the predictors. Thus, for the sake of accuracy, to consider non-linear and non-additive relationships between the predictors and response variables, a basis expansion is used. This is a popular methodology for extending the applicability beyond linearity, more details about basis expansions can be found elsewhere [46]. Then, the transformations of the considered predictors for the estimation model are: the square of the values (e.g., D_o^2, D_i^2), the inverse values (e.g., $1/D_o$, $1/D_i$), all the multiplicative combinations (e.g., $D_o * D_i$, $D_o * t_r$), and the division combinations (e.g., D_o/D_i, D_o/t_r). These transformations were used for simplicity, thus avoiding more complex models since the aim is to provide a simple prediction model. The set of predictors reached a number of 167 (H_r^3 and H_r^5 were included for a_{20} and a_{30}), allowing the consideration of some non-linear relations between the model parameters and the geometrical and material properties. Although the prediction model is based only on physically sound properties, this work aims to find the best possible mathematical representation of the force–deformation relationship of HDRBs. Indeed, this implies a trade-off between the physical meaning of the model and numerical accuracy.

4.2. Optional prediction models

A linear regression was used to develop the prediction model to estimate a single value of parameter Y. The p inputs of the model are grouped in the vector $X^T = (X_1, X_2, \ldots, X_p)$, where X_i is the value of the i-th predictor. The estimation of the parameter Y is expressed as

$$\hat{Y} = \hat{\beta}_0 + \sum_{j=1}^{p} X_j \hat{\beta}_j, \tag{22}$$

where $\hat{\beta}_0$ is the intercept, also known as the bias; and $\hat{\beta} = [\hat{\beta}_j]$ is the p-vector coefficients of the linear regression. The coefficients of vector $\hat{\beta}$ are estimated from the minimization of the Residual Sum of Squares (RSS) and can be explicitly evaluated as [46]

$$\hat{\beta} = (\boldsymbol{X}^T \boldsymbol{X})^{-1} \boldsymbol{X}^T \boldsymbol{Y}, \tag{23}$$

where $\boldsymbol{X}$ is an $N \times p$ matrix with each row corresponding to an input vector, and $\boldsymbol{Y}$ is an N-vector with the measurements of parameter Y, and N is the number of cases (devices) in the dataset. However, considering all 167 predictors to estimate each model parameter would result in models that are too complex and with low accuracy. In statistical terms, this is due to the bias–variance trade-off; linear regressions often have a low bias but high variance. Sometimes, it is better to sacrifice bias marginally to reduce the variance of the prediction [46], resulting in an improved estimation. Moreover, too many predictors generate over-fitting, which limits the generalization of the model. Consequently, it is convenient to select a small subset of predictors capable of representing the relevant behavior of the variables.

The database with 924 devices was divided randomly into two groups: the training data (80%) and the validation data (20%). The former is used in model calibration, while the latter in model validation. A different subset of predictors was selected for each target parameter, which unknowns are the number and predictors to use. This is a non-trivial task due to the large number of variables used and possible combinations. The process of selecting the predictors is commonly known as model selection, and it was performed using the software *R* [47]. The different subsets considered a number of predictors ranging between 0 and 25 to build the prediction models, reaching a universe of 26 models per parameter. In the case of no predictors, the mean of the training dataset is used as the estimation, while for the model with a single predictor, the parameter that minimizes the Mean Squared Error (MSE) Ψ is selected. For the subsets with two and more predictors, the sequential replacement algorithm was used [48]. The basic idea of the method is to select an initial group of predictors randomly and check if replacing any of the ones selected with another, the MSE is reduced. More details about the method can be found elsewhere [48]. All the estimation models used the MSE as a quantifier of the accuracy, which is computed using the expression

$$\Psi = \frac{1}{m} \sum_{i=1}^{m} \left(Y_i - \hat{Y}_i\right)^2, \tag{24}$$

where m is the number of data points.

Fig. 5 shows the MSE with the training (Ψ_{train}) and validation (Ψ_{test}) datasets for all variables. In all cases, the Ψ_{train} decreases as the number of predictors increases, as it should be expected. However, the same is not true for the Ψ_{test}. This is a consequence of the bias–variance trade-off; as the model complexity rises, the bias reduces at a lesser rate than the increase in variance. An interesting feature is that Ψ_{test} is under Ψ_{train} for some variables, which is not a common trend since the estimation model should show a better fit since it uses the training dataset for its calibration. Nonetheless, this is the case due to the partition of the data in these two groups. The training dataset resulted in a larger dispersion than the test dataset; and hence, the Ψ_{train} is larger than the Ψ_{test}.

Table 2
Estimation of the constant value model parameters.

Variable	Value	Variable	Value
C_1	0.640	C_m	0.165
C_2	15.457	η	0.319
p_2	0.304	Φ_{max}	0.233
p_3	0.235	P_Φ	0.008

Table 3
Estimation models for parameters considered as variable.

Variable	Units	Value
a_{10}	tonf	$3.046 + 2.201 H_r K_h$
a_{20}	tonf	$-166.48 + 1.84 H_r^2$
a_{30}	tonf	$1.617 + 0.0003 H_r^5$
p_1	[–]	$0.467 + 1.15 H_r \sigma$
C_3	[–]	$0.722 + 0.241 H_r$
p_m	[–]	$0.209 + 0.0004 P\sigma$
γ_y	[–]	$0.029 - 9.0e^7 H_r^3$
f_y	tonf	$1.667 + 0.00005 PD_o$
β[a]	[–]	$0.86 - 0.008 K_h / H_r$

[a]The values were limited to the range between 0.1 and 0.9.

4.3. Selection of the prediction model

The prediction model selection is based on the minimization of the MSE. However, it is impractical to use a model with a large number of predictors. Thus, the target model aims to achieve two main characteristics: minimum Ψ_{test} (for generalization performance on independent data), and a minimum number of predictors (for minimization of model complexity). Based on the MSE results of the possible prediction models, the model parameters can be split into two groups depending on the number of needed predictors: those with constant value and those truly variable.

A model parameter is considered constant if the Ψ_{test} value of the model using no predictors is smaller than the minimum value of Ψ_{test} plus 10%. This requirement is fulfilled by eight model parameters, which are listed in Table 2. It is worth mentioning that one of the two parameters controlling degradation on each term can be considered constant, with the exception of the term f_{s2} for which both parameters can be considered constant. Additionally, the parameters that control the sharpness of the smooth transition of the force–deformation cycle from the elastic to the inelastic zone, and the temporary hardening can also be considered constant.

The other nine parameters were estimated considering prediction models with a single predictor. Please notice that the prediction model was developed for a shear force response in tonf, thus the estimated values of the parameters a_{10}, a_{20}, a_{30} and f_y are in tonf. Table 3 summarizes the estimation models of these nine parameters, which were estimated using the classical linear regression presented above. Although each parameter shows dependency with different predictors, the total height of rubber, H_r, seems to influence the value of most parameters.

Fig. 6 shows two examples with the data points and the prediction of parameters a_{10} and p_m. Both parameters show significant variability in the results due to the large uncertainty of the force–deformation constitutive behavior of the devices. As a consequence, the experimental results of given single device show significant differences from the numerical results obtained using the estimation model since the latter is intended to estimate the behavior of an average device in a batch. Please notice that the prediction model was developed entirely from a statistical approach, and some relations shown in Table 3 may seem illogical from a physically oriented approach. However, these expressions are the ones that best fit the experimental data.

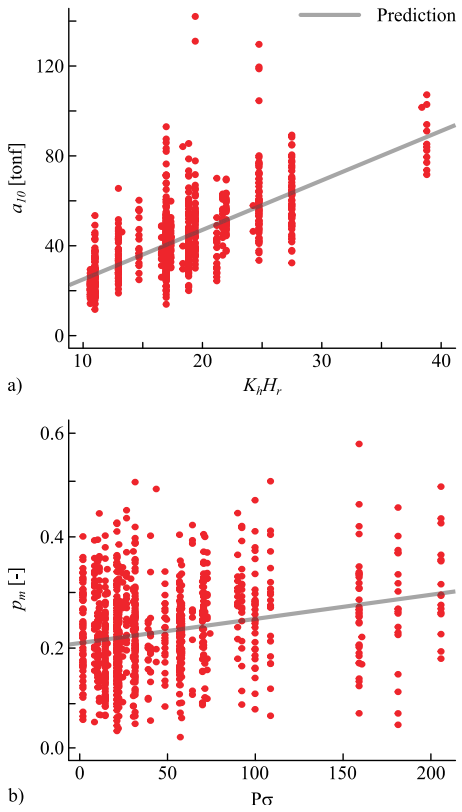

Fig. 6. Example of data points and estimation of model parameters: (a) a_{10}, and (b) p_m.

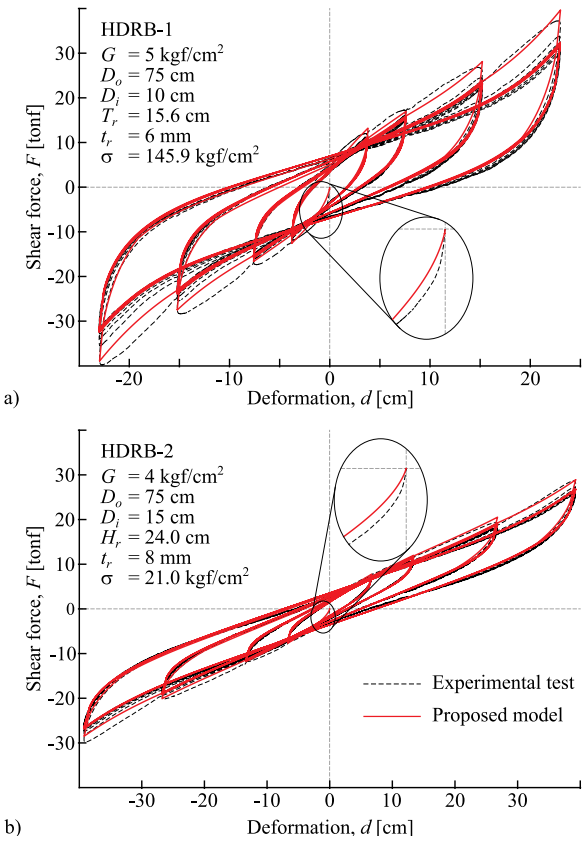

Fig. 7. Force–deformations comparison between numerical (solid line) and experimental responses (dashed line) for two different isolation devices: (a) HDRB-1 and (b) HDRB-2.

5. Validation of the proposed model and results

In this section, the proposed numerical model and the prediction model for the parameters are validated using experimental data. The experimental results correspond to devices subjected to the design axial loads and a specific horizontal cyclic deformation history. So far, since the proposed model neglects the coupling between axial and shear loads, only the horizontal cyclic deformation history was considered for the numerical tests. Three types of results are presented next, two aimed at displaying the capabilities of the model that include: (a) global results to evaluate the accuracy of the model versus the experimental cyclic behavior of HDRBs, and (b) relative comparisons of the accuracy of the proposed model with respect to other three existing numerical models; and another aimed at validating the quality of the predictions of the model parameters through a (c) comparison between the numerical results with the parameter values computed by the prediction model and the experimental results of two sets of devices with different nominal properties.

5.1. Global results

Two annular HDRBs were randomly selected as examples to present the typical accuracy of the model; the benchmark devices were tested for quality control and belong to different building projects. The material and geometric properties are different for both examples to show the capability of the model to simulate the force–deformation response of different devices. The benchmark devices were randomly selected from the dataset of 924 HDRBs, and the resulting model used parameters of the calibration process with the CMA-ES algorithm explained in the previous section.

Fig. 7 compares the numerical responses of the proposed model and the corresponding experimental test results. In both cases, the proposed model represents the behavior of the device with sufficient accuracy, including the effective stiffness, energy dissipation, maximum force, and stiffness degradation. These results are typical of the 924 benchmark devices of the subset, demonstrating that the proposed model represents well the shear behavior of HDRBs. The largest differences between the numerical and experimental results occur for the initial stiffness. The proposed model underestimates this stiffness value since the initial stiffness of the model equals the initial stiffness of each unloading branch. Thus, the calibration algorithm tries to match the unloading stiffness rather than of the initial stiffness of the device.

5.2. Comparison with other numerical models

The accuracy of the proposed model is also compared with other numerical models available in the literature. Three numerical models with different levels of sophistication were used as benchmark. The first is the one proposed by Oliveto et al. [17] ($M1$) for bi-directional shear, which requires the calibration of 16 parameters and consists of seven elements connected in parallel: a nonlinear spring, a bounding surface plasticity element, and five elastoplastic elements. The second is the model proposed by Grant et al. [20] ($M2$), also for bi-directional shear. This model requires the calibration of 10 parameters and decomposes the response into two components working in parallel, an elastic and a hysteretic component. The model includes degradation and stiffening at high strain levels. The third is the numerical model proposed by Tubaldi et al. [21] ($M3$), which needs the calibration of 16 parameters to include stiffness degradation and strain-rate dependency.

Before this comparison, each implementation of the previous analytical models was verified using the examples presented in each reference. Once each code was validated, an arbitrary device was

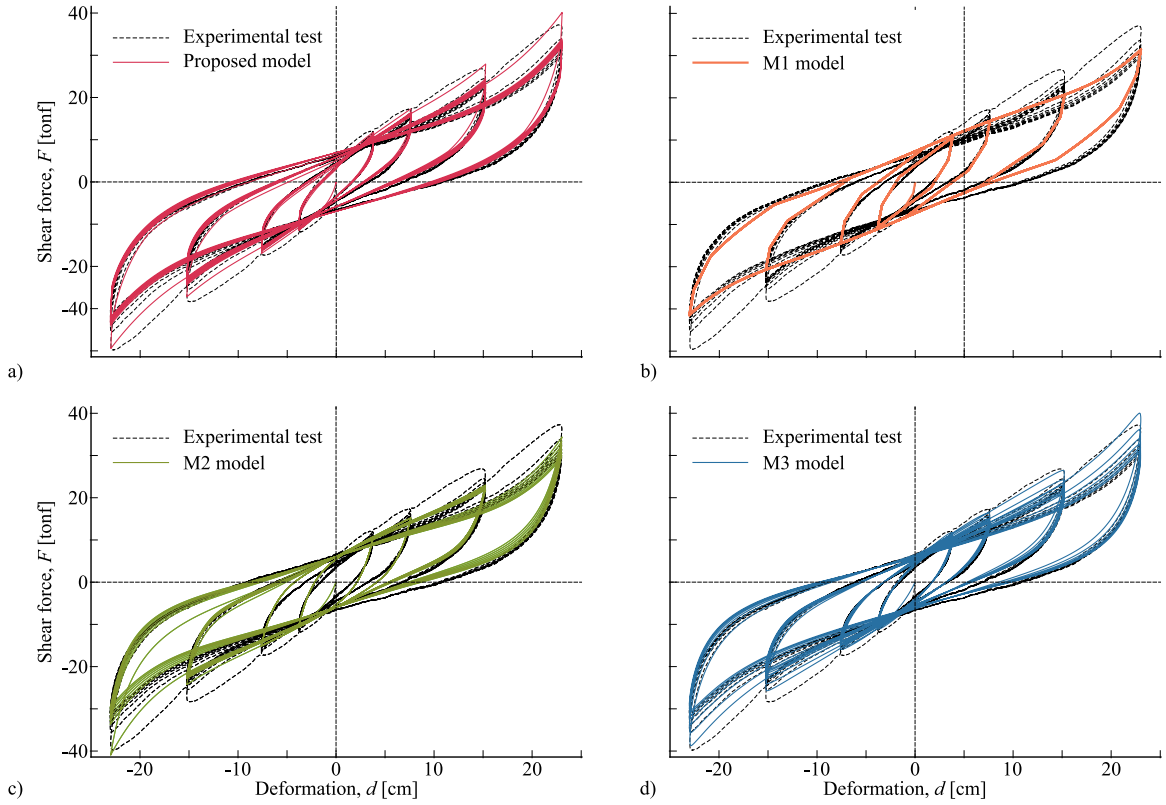

Fig. 8. Comparison of the force–deformation experimental response with (a) the proposed model, and with the previous models in the literature: (b) Oliveto et al. [17] (M1 model); (c) Grant et al. [20] (M2 model); and (d) Tubaldi et al. [21] (M3 model).

Table 4
Quantitative comparison between the different numerical models and experimental test results, measured as the percentage difference.

Model	Ψ	E_T	K_{ini}	E_1	E_5	K_1	K_5
Proposed	0.67	0.67	−59.28	−5.58	2.49	3.11	4.27
$M1$	3.35	4.00	−38.88	−16.44	1.25	−17.96	0.66
$M2$	2.08	−6.41	−72.21	−27.45	−12.72	−2.34	−1.78
$M3$	0.70	−1.31	−76.50	−5.13	−1.10	−1.62	4.20

chosen from our database and used in the comparison. The set of parameters for each model, including the parameters for the proposed model, was calibrated using the CMA-ES algorithm [42] using the same parameters as described previously for the optimization algorithm. It is important to mention that the set of parameters for each model may not necessarily be the optimal set, including the case of our proposed model, since the algorithm may find a local minimum for the RSS during the optimization process.

Fig. 8 shows the comparison of the proposed and the other three numerical models with the experimental results of a benchmark device. Visual inspection shows that the proposed model fits better the experimental test results than the other three numerical models. The $M1$ tries to match the shape of the force–deformation response but does not incorporate stiffness degradation and has a non-smooth unloading curve. The advantage of this model, though, is its computing time, which is the lowest among all four models. The $M2$ model shows good agreement in the shape of the unloading curve; however, it does not incorporate the unilateral effect, i.e., scragging is only present in the first half cycle of each strain level. In addition, since the parameter that controls the stiffness degradation evolves only during unloading, the force estimates present a sharp increase in the first cycle of the last shear deformation level. Another small disadvantage of this model is present in the transition zone, where the unloading of the first cycle leads to larger values than the experimental results, this is clearly shown in the largest strain level. The $M3$ model also fits reasonably well the experimental response. Differences can be found in the initial stiffness and stiffness degradation. The former is significantly underestimated, and the latter is not captured properly in all cycles, since the model underestimates the stiffness degradation between the first and second cycles.

Seven response parameters were measured to evaluate the accuracy of the models quantitatively: MSE of the forces Ψ, total dissipated energy E_T, initial stiffness K_{ini}, dissipated energy during the first and fifth cycles of the maximum strain levels (E_1 and E_5, respectively), and secant stiffness at the first and fifth cycles of the maximum strain levels (K_1 and K_5, respectively). The secant stiffness and energy dissipated per cycle were chosen since they are the most used parameters in design. Also, the first and fifth cycles were considered to account for the behavior before and after scragging. The aim of this comparison is to roughly quantify the overall difference between the numerical models and the experimental test results. The percentage difference was used for all response parameters with the exception of the MSE.

Table 4 presents the numerical results of the comparison. The proposed model gets the minimum MSE (Ψ) with a value of 0.67, followed closely by M3, and with larger differences for M2, and M1, respectively. In terms of total dissipated energy (E_T), the proposed model is the best at simulating the experimental results, with an error value of 0.67%, while the model $M3$ is the second, underestimating the total energy dissipating by 1.31%. Considering the errors of dissipated energy during single cycles (E_1, E_5), the proposed and $M3$ models show smaller differences than the other two models, with values up to 6%. Thus, both models can effectively simulate the dissipated energy at every single cycle. The $M1$ model is the only one which error in secant stiffness is larger than 5% (K_1). It occurs for the first cycle and is a consequence of the model that does not include stiffness degradation. The initial stiffness (K_{ini}) is the parameter with larger estimation errors. All models underestimated the value of this parameter, but the best

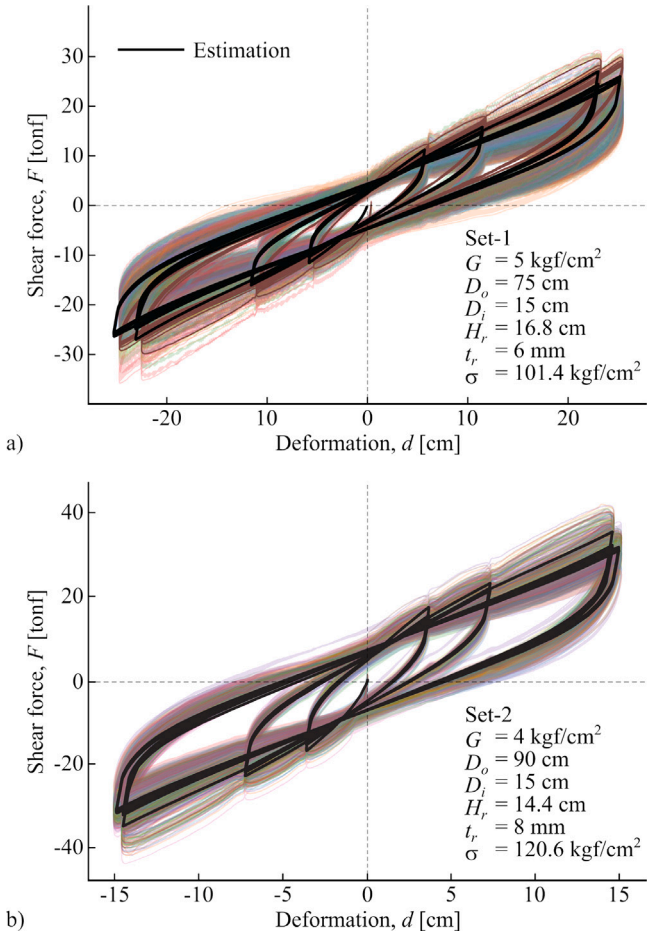

Fig. 9. Force–deformation cycle comparisons using the estimated values of the proposed numerical model (solid black line) with experimental test results (colored lines) of (a) Set-1 and (b) Set-2.

estimation is produced by $M1$, followed by the proposed model, with values of −38.88 and −59.28%, respectively. This quantitative comparison shows that the proposed model is reasonably accurate and provides a balanced error between all the considered parameters.

5.3. Overall results of the prediction model

The prediction for the model parameters, which was presented in the previous section, was evaluated using two sets of independent tests of devices that were not considered in the model development and its calibration. These validation sets come from the experimental results of the production testing of accepted devices for other two different building projects. The sets are denoted as Set-1 and Set-2, which include results of 66 and 77 HDRBs, respectively.

Fig. 9 shows a comparison between the force–deformation cyclic results of the proposed numerical model using the parameter values of the estimated model presented in the previous section, and two new sets of experimental test results. The sets of experimental results show large variability, which can be seen clearly in Figs. 9a and 9b. All devices of each test were manufactured with the same nominal materials and geometrical properties, and were tested using the same load pattern. The variability of the force–deformation response is mainly due to the intrinsic variability of the mechanical properties of the rubber material and the manufacturing process. It is well known that the rheological properties of the elastomeric compound are extremely sensitive to temperature and pressure, as well as the time of curing. The misalignment of the steel shims also influences its lateral and vertical behavior. The numerical model using the estimated parameters represents the behavior of an average device of both sets of devices reasonably well. The estimated response fits well the initial stiffness, energy dissipation capacity, and degradation observed in the experimental results, demonstrating that it can be used for the simulation of general HDRBs under dynamic and static loads.

6. Numerical implementation

The source code for the proposed model is available at https://github.com/JAGallardo1992/HDRB_model. The repository includes the Python and Matlab implementations, and an example with the experimental response for an HDRB.

7. Summary and conclusions

This work proposes a new force–deformation phenomenological constitutive model for HDRBs. The model consists of two components connected in parallel, a hyperelastic spring and a dissipative element. The former includes anisotropic stiffness degradation (scragging and Mullins effect), while the latter considers temporary hardening. The results on a large database of 924 devices demonstrate that the proposed model can accurately simulate the cyclic behavior of HDRBs. Also, the statistical procedure performed to establish the variables of the prediction model show that eight of the seventeen parameters of the model can be considered constant, while the other nine need to be estimated from the geometric and material properties of the devices. The estimation model can simulate the behavior of an average device of a batch of nominally identical HDRBs. The necessary information for estimating the model parameter values is included. The main conclusions of this research are:

- The model is capable of accurately simulating anisotropic degradation, as well as temporary hardening, phenomena that have been ignored by several of the previous numerical models. Another important feature of the proposed model is that the scragging control variable evolves in the loading branch (Eq. (18)), thus avoiding a sharp growth of the shear force in the first cycle at large strain levels. Although the number of model parameters is large (17), only nine require calibration, making it simpler to calibrate with experimental data.
- The proposed model was also tested against three existing alternative HDRB models showing slightly better performance for the data set considered herein. The proposed model also includes the unilateral effect and the temporary hardening, which is not commonly present in existent models.
- The parameter estimation model presented in Section 4 is derived from a statistical approach, which implies a trade-off between physical meaning and numerical accuracy. Thus, some relations among parameters have no physical meaning, but they represent the best-fit models for the experimental data. All other physically-based relations provided poorer numerical estimations for the same model parameter values.
- The available experimental data of nominal identical devices shows significant uncertainty in the force–deformation response. The material, as well as the manufacturing process, are both important sources to explain variability in the response. Naturally, part of this uncertainty in the test results can also be attributed to the measurement procedure and the experimental setup [29]. No matter the source, the inherent uncertainty of the devices should be taken into account in the analysis of isolated structures. This is particularly important since the nonlinear behavior of the building strongly depends on the behavior of the isolation system. This variability may induce a relevant variation in the shear forces, accelerations, and floor displacements.

CRediT authorship contribution statement

José A. Gallardo: Conceptualization, Methodology, Investigation, Software, Validation. **Juan C. de la Llera:** Conceptualization, Writing – review & editing, Supervision, Funding acquisition. **José I. Restrepo:** Validation, Supervision. **Michelle Chen:** Validation, Writing – review & editing.

Declaration of competing interest

The authors declare that they have no known competing financial interests or personal relationships that could have appeared to influence the work reported in this paper.

Data availability

Data will be made available on request.

Acknowledgments

This research has been sponsored by ANID, under the projects: ANID/doctorate scholarship/ 21201370; Research Center for Integrated Disaster Risk Management (CIGIDEN), ANID/ FONDAP/ 1522A0005; and FONDECYT project, Multiscale earthquake risk mitigation of healthcare networks using seismic isolation, ANID/ FONDECYT/ 1220292.

References

[1] Mokha AS, Amin N, Constantinou MC, Zayas V. Seismic isolation retrofit of large historic building. J Struct Eng 1996;122(3):298–308. http://dx.doi.org/10.1061/(ASCE)0733-9445(1996)122:3(298).
[2] Matsagar VA, Jangid R. Base isolation for seismic retrofitting of structures. Pract Period Struct Des Constr 2008;13(4):175–85. http://dx.doi.org/10.1061/(ASCE)1084-0680(2008)13:4(175).
[3] D'amato M, Gigliotti R, Laguardia R. Seismic isolation for protecting historical buildings: A case study. Front Built Environ 2019;5:87. http://dx.doi.org/10.3389/fbuil.2019.00087.
[4] De la Llera JC, Lüders C, Leigh P, Sady H. Analysis, testing, and implementation of seismic isolation of buildings in Chile. Earthq Eng Struct Dyn 2004;33(5):543–74. http://dx.doi.org/10.1002/eqe.360.
[5] Fujita T. Demonstration of effectiveness of seismic isolation in the Hanshin-Awaji earthquake and progress of applications of base-isolated buildings. Technical report, University of Tokyo; 1995.
[6] De La Llera J, Mitrani-Reiser J, Rivera Jofre F, Fortuño C, Jünemann R, Poulos A, Vásquez J. The 2010 Chile earthquake: a five year reflection. In: Proceedings of the 10th pacific conference on earthquake engineering. AEES; 2015, p. 210.
[7] Kelly JM. Earthquake-resistant design with rubber. Springer; 1993.
[8] Fenz DM, Constantinou MC. Behaviour of the double concave friction pendulum bearing. Earthq Eng Struct Dyn 2006;35(11):1403–24. http://dx.doi.org/10.1002/eqe.589.
[9] Becker TC, Mahin SA. Experimental and analytical study of the bi-directional behavior of the triple friction pendulum isolator. Earthq Eng Struct Dyn 2012;41(3):355–73. http://dx.doi.org/10.1002/eqe.1133.
[10] Lee D, Constantinou MC. Quintuple friction pendulum isolator: behavior, modeling, and validation. Earthq Spectra 2016;32(3):1607–26. http://dx.doi.org/10.1193/040615EQS053M.
[11] Pinochet J, De la Llera JC, Lüders C. Analysis of a kinematic self-centring seismic isolator. Earthq Eng Struct Dyn 2006;35(12):1533–61. http://dx.doi.org/10.1002/eqe.601.
[12] Wang B, Zhu S, Casciati F. Experimental study of novel self-centering seismic base isolators incorporating superelastic shape memory alloys. J Struct Eng 2020;146(7):04020129. http://dx.doi.org/10.1061/(ASCE)ST.1943-541X.0002679.
[13] Kumar M, Whittaker AS, Constantinou MC. An advanced numerical model of elastomeric seismic isolation bearings. Earthq Eng Struct Dyn 2014;43(13):1955–74. http://dx.doi.org/10.1002/eqe.2431.
[14] Markou AA, Manolis GD. Mechanical models for shear behavior in high damping rubber bearings. Soil Dyn Earthq Eng 2016;90:221–6. http://dx.doi.org/10.1016/j.soildyn.2016.08.035.
[15] Maureira N, de la Llera J, Oyarzo C, Miranda S. A nonlinear model for multilayered rubber isolators based on a co-rotational formulation. Eng Struct 2017;131:1–13. http://dx.doi.org/10.1016/j.engstruct.2016.09.055.
[16] Ishii K, Kikuchi M. Improved numerical analysis for ultimate behavior of elastomeric seismic isolation bearings. Earthq Eng Struct Dyn 2019;48(1):65–77. http://dx.doi.org/10.1002/eqe.3123.
[17] Oliveto ND, Markou AA, Athanasiou A. Modeling of high damping rubber bearings under bidirectional shear loading. Soil Dyn Earthq Eng 2019;118:179–90. http://dx.doi.org/10.1016/j.soildyn.2018.12.017.
[18] Miranda S, Miranda E, de la Llera JC. A simplified and versatile element model for elastomeric seismic isolation bearings. Earthq Spectra 2021;87552930211030939. http://dx.doi.org/10.1177/87552930211030939.
[19] Kikuchi M, Aiken ID. An analytical hysteresis model for elastomeric seismic isolation bearings. Earthq Eng Struct Dyn 1997;26(2):215–31. http://dx.doi.org/10.1002/(SICI)1096-9845(199702)26:2<215::AID-EQE640>3.0.CO;2-9.
[20] Grant DN, Fenves GL, Whittaker AS. Bidirectional modelling of high-damping rubber bearings. J Earthq Eng 2004;8(spec01):161–85. http://dx.doi.org/10.1142/S136324690400164X.
[21] Tubaldi E, Ragni L, Dall'Asta A, Ahmadi H, Muhr A. Stress softening behaviour of HDNR bearings: modelling and influence on the seismic response of isolated structures. Earthq Eng Struct Dyn 2017;46(12):2033–54. http://dx.doi.org/10.1002/eqe.2897.
[22] ASCE/SEI7-16. Minimum design loads and associated criteria for buildings and other structures. American Society of Civil Engineers; 2017, http://dx.doi.org/10.1061/9780784414248.
[23] Ministero delle infrastrutture e dei trasporti. Norme tecniche per le costruzioni. Italian Tech Norms Constr 2018. (In Italian).
[24] British Standards Institution. Eurocode 8: Design of structures for earthquake resistance-part 1: general rules, seismic actions and rules for buildings. Brussels: Eur Committee Standardization 2005.
[25] Gheryani MH, Razak HA, Jameel M. Dynamic response changes of seismic isolated building due to material degradation of HDRB. Arab J Sci Eng 2015;40(12):3429–42. http://dx.doi.org/10.1007/s13369-015-1794-7.
[26] Kodakkal A, Saha SK, Sepahvand K, Matsagar VA, Duddeck F, Marburg S. Uncertainties in dynamic response of buildings with non-linear base-isolators. Eng Struct 2019;197:109423. http://dx.doi.org/10.1016/j.engstruct.2019.109423.
[27] Cardone D, Perrone G, Piesco V. Developing collapse fragility curves for base-isolated buildings. Earthq Eng Struct Dyn 2019;48(1):78–102. http://dx.doi.org/10.1002/eqe.3126.
[28] Flora A, Perrone G, Cardone D. Evaluating collapse fragility curves for existing buildings retrofitted using seismic isolation. Appl Sci 2020;10(8):2844. http://dx.doi.org/10.3390/app10082844.
[29] Miranda S, de la Llera JC, Miranda E. Uncertainty on measurement of elastomeric isolators effective properties. Measurement 2021;180:109511. http://dx.doi.org/10.1016/j.measurement.2021.109511.
[30] Mullins L. Softening of rubber by deformation. Rubber Chem Technol 1969;42(1):339–62. http://dx.doi.org/10.5254/1.3539210.
[31] Chen MC, Restrepo JI, Benzoni G. Response of a high damping rubber bearing to multiaxial excitation. J Test Eval 2019;49(2):1153–72.
[32] Dorfmann A, Burtscher SL. Aspects of cavitation damage in seismic bearings. J Struct Eng 2000;126(5):573–9. http://dx.doi.org/10.1061/(ASCE)0733-9445(2000)126:5(573).
[33] Gent AN. Engineering with rubber: how to design rubber components. Carl Hanser Verlag GmbH Co KG; 2012.
[34] Koh CG, Kelly JM. A simple mechanical model for elastomeric bearings used in base isolation. Int J Mech Sci 1988;30(12):933–43. http://dx.doi.org/10.1016/0020-7403(88)90075-6.
[35] Ryan KL, Kelly JM, Chopra AK. Nonlinear model for lead–rubber bearings including axial-load effects. J Eng Mech 2005;131(12):1270–8. http://dx.doi.org/10.1061/(ASCE)0733-9399(2005)131:12(1270).
[36] Gent AN. Elastic stability of rubber compression springs. J Mech Eng Sci 1964;6(4):318–26.
[37] Holzapfel GA. Nonlinear solid mechanics: a continuum approach for engineering. John Wiley and Sons; 2000.
[38] Tadmor EB, Miller RE, Elliott RS. Continuum mechanics and thermodynamics: from fundamental concepts to governing equations. Cambridge University Press; 2012.
[39] Mooney M. A theory of large elastic deformation. J Appl Phys 1940;11(9):582–92.
[40] Rivlin R. A note on the torsion of an incompressible highly-elastic cylinder. In: Mathematical proceedings of the cambridge philosophical society, vol. 45. Cambridge University Press; 1949, p. 485–7.
[41] Karavasilis TL, Kerawala S, Hale E. Hysteretic model for steel energy dissipation devices and evaluation of a minimal-damage seismic design approach for steel buildings. J Construct Steel Res 2012;70:358–67. http://dx.doi.org/10.1016/j.jcsr.2011.10.010.
[42] Hansen N, Ostermeier A. Completely derandomized self-adaptation in evolution strategies. Evolutionary Computation 2001;9(2):159–95. http://dx.doi.org/10.1162/106365601750190398.
[43] Hansen N. The CMA evolution strategy: A tutorial. 2016, http://dx.doi.org/10.48550/arXiv.1604.00772, arXiv preprint arXiv:1604.00772.

[44] Athanasiou A, De Felice M, Oliveto G, Oliveto PS. Evolutionary algorithms for the identification of structural systems in earthquake engineering. In: IJCCI (ECTA-FCTA). 2011, p. 52–62.
[45] Athanasiou A, Felice MD, Oliveto G, Oliveto PS. Dynamical modeling and parameter identification of seismic isolation systems by evolution strategies. In: Computational intelligence. Springer; 2013, p. 101–18.
[46] Friedman J, Hastie T, Tibshirani R, et al. The elements of statistical learning, vol. 1. Springer series in statistics New York; 2001.
[47] RCore Team. R: A language and environment for statistical computing. 2020, URL www.R-project.org/.
[48] Miller A. Subset selection in regression. CRC Press; 2002.